Article

Giant stress response of terahertz magnons in a spin-orbit Mott insulator

Hun-Ho Kim[1], Kentaro Ueda [1,2], Suguru Nakata [1], Peter Wochner[1], Andrew Mackenzie [3,4], Clifford Hicks [3,5], Giniyat Khaliullin [1], Huimei Liu[1,6] ✉, Bernhard Keimer [1] ✉ & Matteo Minola [1] ✉

Magnonic devices operating at terahertz frequencies offer intriguing prospects for high-speed electronics with minimal energy dissipation However, guiding and manipulating terahertz magnons via external parameters present formidable challenges. Here we report the results of magnetic Raman scattering experiments on the antiferromagnetic spin-orbit Mott insulator Sr_2IrO_4 under uniaxial stress. We find that the energies of zone-center magnons are extremely stress sensitive: lattice strain of 0.1% increases the magnon energy by 40%. The magnon response is symmetric with respect to the sign of the applied stress (tensile or compressive), but depends strongly on its direction in the IrO_2 planes. A theory based on coupling of the spin-orbit-entangled iridium magnetic moments to lattice distortions provides a quantitative explanation of the Raman data and a comprehensive framework for the description of magnon-lattice interactions in magnets with strong spin-orbit coupling. The possibility to efficiently manipulate the propagation of terahertz magnons via external stress opens up multifold design options for reconfigurable magnonic devices.

In recent years, $4d$ and $5d$ transition metal oxides have been extensively investigated in the search for novel electronic phases [1,2]. In these compounds, the spin–orbit coupling (SOC) is comparable to other relevant interactions, such as the exchange and Jahn-Teller couplings, and therefore not treatable as a small perturbation as it is in $3d$-electron compounds. Instead, spin–orbit-entangled states comprising various d-orbitals with a different spin and orbital quantum numbers are formed. These states are represented by an effective ("pseudo") spin $\tilde{J}$ [3]. The pseudospins have a large orbital contribution and thus generate a nontrivial structure of the orbital interactions, which are bond-directional and highly susceptible to crystal field environments [4]. This leads to the realization of various exotic magnetic ground states, such as the Kitaev spin-liquid on the honeycomb lattice [5–9] and the all-in-all-out magnetic structure on the pyrochlore lattice [10–12], with

corresponding collective excitations in the terahertz range. A major frontier of current research seeks to understand and control the confluence of spin–orbit, spin-lattice, and exchange interactions that determines the nature of these excitations, and to harness them for device applications.

The Mott-insulating square-lattice iridate Sr_2IrO_4 has emerged as a model system for spin–orbit-entangled magnetism and has drawn broad attention as a rare example of the quasi-two-dimensional Heisenberg antiferromagnet, a concept that is of key importance for the cuprate high-T_c superconductors [13]. In this compound, Ir^{4+} ions with t_{2g}^5 configuration possess spin $S = 1/2$ and an effective orbital moment $\tilde{L} = 1$, which are coupled by a large SOC ($\xi \simeq 0.4$ eV), forming a pseudospin $\tilde{J} = 1/2$ [14]. Below $T_N = 240$ K, Sr_2IrO_4 shows canted in-plane antiferromagnetic order. Resonant inelastic x-ray scattering experiments [15]

[1]Max Planck Institute for Solid State Research, Heisenbergstraße 1, D-70569 Stuttgart, Germany. [2]Department of Applied Physics, The University of Tokyo, Bunkyo-ku, Tokyo 113-8656, Japan. [3]Max Planck Institute for Chemical Physics of Solids, Nöthnitzer Straße 40, D-01187 Dresden, Germany. [4]SUPA, School of Physics and Astronomy, University of St. Andrews, St. Andrews KY16 9SS, United Kingdom. [5]School of Physics and Astronomy, University of Birmingham, Birmingham B15 2TT, United Kingdom. [6]Leibniz Institute for Solid State and Materials Research Dresden IFW, Helmholtzstraße 20, D-01069 Dresden, Germany. ✉e-mail: huimei.liu@ifw-dresden.de; b.keimer@fkf.mpg.de; m.minola@fkf.mpg.de
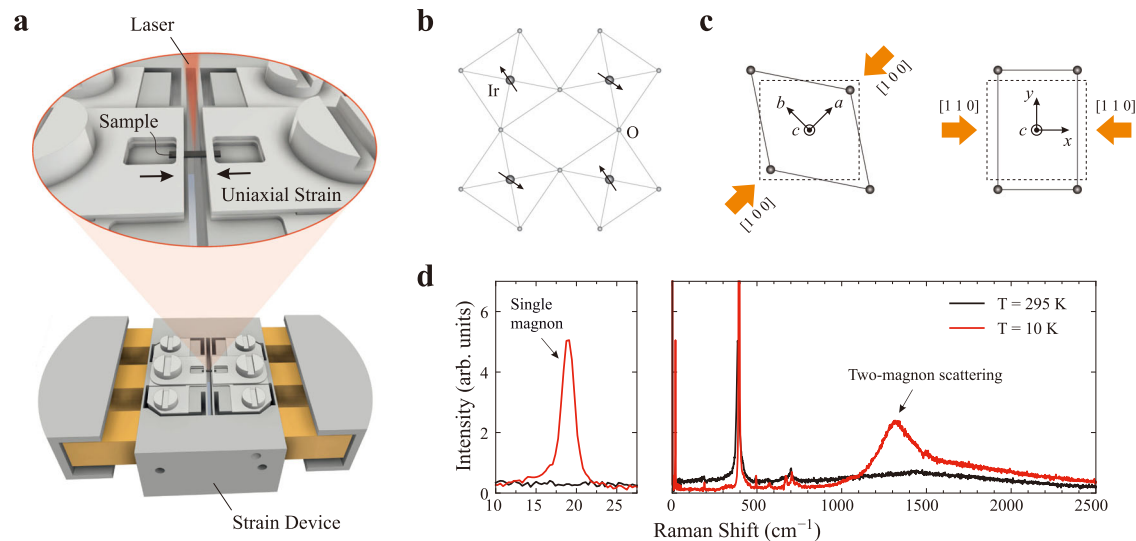
Fig. 1 | Measurement setup for uniaxial strain experiments. a Schematic picture of the experimental geometry with the strain device. **b** Sketch of the crystal and magnetic structure of an IrO_2 plane. Black (gray) circles represent Ir (O) atoms. Black arrows represent pseudospins. **c** Orthorhombic deformations of xy type (left, strain along the [1 0 0] direction) and $x^2 - y^2$ type (right, strain along the [1 1 0]

direction). Solid (dashed) lines represent the strained (undistorted) lattice. Orange arrows show the applied stress directions. **d** Raman spectra of B_{2g} symmetry measured below and above T_N. The left panel shows the low-energy range, where a single-magnon peak is observed below T_N.

revealed magnon excitations with energies up to 50 THz, comparable to those in the cuprates.

Whereas the overall energy scale in Sr_2IrO_4 is dictated by the isotropic Heisenberg coupling, higher-order interactions are crucial for understanding its low-energy magnetic properties. For example, Dzyaloshinskii–Moriya and XY-type exchange anisotropy terms[6] are instrumental to describe the weak ferromagnetism and magnetic critical scattering data[16]. However, these interactions do not uniquely determine the staggered moment direction in a crystal. Experimentally, the pseudospins are oriented along the [1 0 0] axis, i.e., 45° away from the Ir-O-Ir bond direction[14,17]. Raman[18,19] and inelastic neutron scattering experiments[20] detected a magnon gap of ~0.5 THz associated with the magnetic anisotropy within the xy-plane. The nature of the interactions breaking the XY-symmetry in Sr_2IrO_4 remains unresolved to-date. In principle, pseudodipolar-type couplings[6] can open a magnon gap via an order-by-disorder mechanism as in the cuprates[21,22], but this would align the moments parallel to the Ir-O-Ir bond direction, inconsistent with the experiment.

There have been several theoretical attempts to clarify the origin of the in-plane anisotropy in Sr_2IrO_4. Katukuri et al.[23] suggested that the anisotropic interlayer couplings might be relevant, whereas ref. 24 proposed a mechanism involving orbital-lattice coupling. Via spin–orbit entanglement, this coupling is transformed into a pseudospin-lattice interaction, which breaks the tetragonal symmetry and generates an in-plane anisotropy. A small orthorhombic distortion below T_N was predicted based on this model. On the experimental front, various manifestations of the pseudospin-lattice interaction in iridates have recently been reported[25–27]. Decisive experimental evidence that establishes a clean, solid connection between the theory and experiments is, however, still lacking.

Here we provide direct evidence that pseudospin-lattice coupling is responsible for the in-plane magnetic anisotropy in Sr_2IrO_4, by tuning the magnon gap using in-situ uniaxial strain. Raman spectroscopy is particularly suitable for this purpose, thanks to its capability to detect subtle energy shifts with ~1 GHz energy resolution, combined with the experimental flexibility to combine spectroscopic measurements with uniaxial strain techniques at cryogenic temperatures. We performed Raman scattering experiments on single crystals of Sr_2IrO_4 under the uniaxial strain along different crystallographic directions.

We found that the magnon gap is remarkably sensitive to small levels of strain. The effect is highly anisotropic and it is symmetric with respect to the sign of the strain, indicating an intimate connection between the in-plane anisotropy and the orthorhombicity. We present a theory that describes our experimental data in quantitative detail and evaluates the intrinsic orthorhombic distortion in Sr_2IrO_4 induced by pseudospin-lattice coupling.

Results

For strain control, we employed a modified version of the piezoelectric-based strain device successfully utilized in several studies of correlated-electron systems[28–33]. Figure 1a shows a schematic picture of the experimental geometry (see Methods for details). We chose two different geometries with uniaxial strain along [1 0 0] and [1 1 0], as shown in Fig. 1c. The strain levels were first estimated using a built-in displacement sensor during the Raman measurements, and later recalibrated by comparison to intrinsic observables measured at each displacement value. To this end, we carried out separate measurements of the energies of selected phonons and of the positions of selected in-plane Bragg reflection by Raman and x-ray scattering, respectively (See Supplementary Note 1 for the strain calibration procedure). Throughout this article, we use the convention of Fig. 1c to represent the crystallographic directions and the polarization geometry.

Figure 1d shows magnetic Raman spectra with B_{2g} symmetry. Well below T_N ~240 K, where the pseudospins align antiferromagnetically as illustrated in Fig. 1b, we observe a sharp single-magnon peak at 18 cm^{-1} (0.54 THz) and a broad two-magnon scattering signal centered at 1300 cm^{-1} (39 THz), which had already been identified in the literature[18,19,25,34]. Figure 2 displays Raman spectra of single-magnon excitations at the zone center under uniaxial strain applied along the [1 0 0] and [1 1 0] axes. Under compressive strain along [1 0 0], the single-magnon energy increases markedly and monotonically, as shown in Fig. 2a. The peak is still clearly visible at $\varepsilon_{[100]} = -0.14\%$, although it broadens slightly and loses some of its intensity with increasing strain. Similar results are found under the tensile strain along the same direction (Fig. 2b).

Remarkably, small levels of compressive strain along [1 1 0] barely affect the magnon energy, as illustrated in Fig. 2c. At larger strain
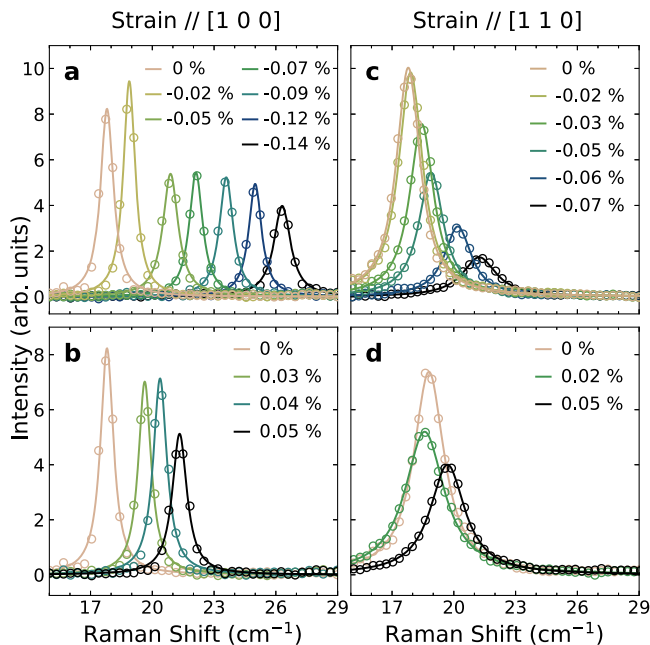
Fig. 2 | Raman spectra of single-magnon excitations under uniaxial strain.
Background-subtracted low-energy Raman spectra were measured under
a compressive and **b** tensile strain along the [1 0 0] direction and under
c compressive and **d** tensile strain along the [1 1 0] direction. Solid lines are the
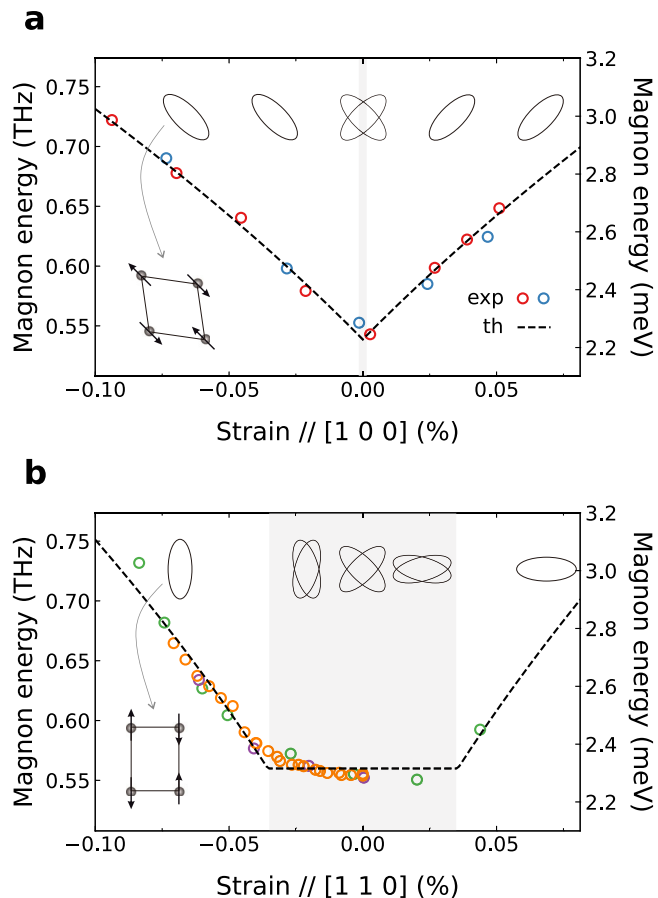results of Lorentzian fits to the data.

Fig. 3 | Response of magnon energies to uniaxial stress. Magnon energy as a
function of uniaxial strain along the **a** [1 0 0] and **b** [1 1 0] axes. Circles with different
colors represent data points measured from different samples. They are vertically
shifted by the following magnitudes (in THz): red(0), blue(0.02), green(0),
orange(0.02), and magenta(0.04). Different vertical shifts are likely due to slightly
different sample qualities. Dashed lines are derived from the pseudospin-lattice
coupling theory. Ellipses represent (exaggerated) orthorhombically-distorted
magnetic domains, as illustrated on the lower left side of each figure. Two ellipses
on top of each other correspond to two degenerate domains, coexisting in the
shaded regions.

values, $|\varepsilon_{[110]}|>0.03\%$, the magnon energy increases notably, as in the
case of [1 0 0] strain. Further increasing strain leads to rapid sup-
pression of the peak intensity and significant broadening of the peak.
Tensile strain along [1 1 0] induces a similar behavior, as shown in
Fig. 2d. Overall, the magnon peak is extremely sensitive to ortho-
rhombic deformation, as an external strain of 0.1% increases the mag-
non energy by almost 40%. This finding clearly demonstrates an
intimate connection between the in-plane magnetic anisotropy and
the lattice deformation.

Figure 3 summarizes the dependence of the magnon energy on
strain along different directions. Note that the magnon response is
symmetric against the strain sign, i.e., the response to compressive
and tensile strain is identical within the experimental error. This
observation rules out any influence of interlayer interactions via
expansion (contraction) of the lattice along the out-of-plane
direction due to the Poisson ratio in response to in-plane com-
pressive (tensile) strain[23]. In this scenario, the resulting change of
the interlayer coupling and magnon energies should be monotonic
functions of the out-of-plane lattice constant and hence antisym-
metric with respect to the strain sign, in contrast to our
observations.

We now show that the above symmetry, as well as the strong
dependence of the magnon gap on the strain direction, are consistent
with the pseudospin-lattice coupling picture. Although lattice distor-
tions cannot lift the Kramers degeneracy of the $\widetilde{J}=1/2$ doublet, they
modify the orbital content of the pseudospin wavefunctions via the
admixture of higher-level states by Jahn-Teller coupling. As a result,
new terms are generated in the exchange Hamiltonian. For uniform
orthorhombic deformations $\varepsilon_1 = (b-a)/(b+a)$ and $\varepsilon_2 = (y-x)/(y+x)$
(depicted in Fig. 1c), they read[24]:

$$\mathcal{H}_{s-l} = g_1\varepsilon_1 (S_i^x S_j^y + S_i^y S_j^x) + g_2\varepsilon_2 (S_i^x S_j^x - S_i^y S_j^y). \quad (1)$$

Hereafter, the pseudospin $\widetilde{J}$ is denoted by $S = 1/2$ for simplicity. One can
interpret $\mathcal{H}_{s-l}$ as a coupling between the distortions $(\varepsilon_1, \varepsilon_2)$ and

pseudospin quadrupole moments (Q_1, Q_2), with $Q_1 = (S_i^x S_j^y + S_i^y S_j^x)$ and
$Q_2 = (S_i^x S_j^x - S_i^y S_j^y)$ of xy and $x^2 - y^2$ symmetries, correspondingly. The
quadrupoles Q_γ ($\gamma \in 1, 2$) reside on the nearest-neighbor exchange
bonds $\langle ij \rangle$, and their amplitude is determined by short-range magnetic
correlations. The constants g_γ depend on Jahn-Teller and SOC
parameters[24].

We define the staggered moment as $\vec{n} = S(\cos\alpha, \sin\alpha)$, with
$\alpha = 0$ corresponding to the Ir-O-Ir bond direction. This gives
$(Q_1, Q_2) = -S^2(\sin 2\alpha, \cos 2\alpha)$ per bond classically, and we obtain
the pseudospin-lattice coupling energy (per site) in the following
form:

$$E_{s-l} = -2S^2 (g_1\varepsilon_1 \sin 2\alpha + g_2\varepsilon_2 \cos 2\alpha). \quad (2)$$

The linear dependence $E_{s-l} \propto \varepsilon_\gamma$ implies structural instability. Minimiz-
ing Eq. (2) together with the elastic energy of the lattice, $\frac{1}{2}K_\gamma\varepsilon_\gamma^2$, one
finds the orthorhombic distortions

$$\varepsilon_1 = \frac{\Gamma_1}{g_1}\sin 2\alpha, \quad \varepsilon_2 = \frac{\Gamma_2}{g_2}\cos 2\alpha, \quad (3)$$

where $\Gamma_\gamma = 2S^2 g_\gamma^2 / K_\gamma$. The total energy as a function of the moment direction α then reads:

$$E = -\Gamma_1 S^2 + (\Gamma_1 - \Gamma_2) S^2 \cos^2 2\alpha. \qquad (4)$$

When $\Gamma_1 > \Gamma_2$, the anisotropy energy E is minimized at $\alpha = 45°$ or $135°$ (i.e., two types of domains), which corresponds to the case of Sr_2IrO_4[14,35]. The resulting distortion, which we denote as ε_0 below, is of xy symmetry and equal to the ε_1 value at $\alpha = 45°$, i.e., $\varepsilon_0 = \Gamma_1/g_1$. This type of orthorhombic distortion is natural for perovskites, as it does not affect the metal-oxygen-metal bond length.

The magnon gap due to the intrinsic deformation ε_0, caused by pseudospin-lattice coupling, is given by[24]:

$$\Delta_0 = 8S \sqrt{J \Gamma_1} = 8S \sqrt{J g_1 \varepsilon_0}, \qquad (5)$$

which is about 0.51–0.58 THz[18,19,26].

External strain ε affects the deformation pattern and thus the magnon energy. Strain applied along the [1 0 0] direction preserves the xy-type symmetry of the intrinsic distortion ε_0 and hence simply enhances its amplitude (as soon as one of the two degenerate domains is selected by a very small external strain). As a result, the magnon gap increases monotonically as a function of ε:

$$\Delta(\varepsilon \parallel [1\,0\,0]) = 8S \sqrt{J g_1 (\varepsilon_0 + |\varepsilon|)} = \Delta_0 \sqrt{1 + \frac{|\varepsilon|}{\varepsilon_0}}. \qquad (6)$$

This dependence is in excellent agreement with the experimental data (Fig. 3a). From corresponding fits, we obtain the magnon gap and intrinsic distortion values in Sr_2IrO_4:

$$\Delta_0 = 0.54 \text{ THz}, \qquad \varepsilon_0 = 1.18 \times 10^{-3}. \qquad (7)$$

Assuming $J \sim 24$ THz[15,36], we evaluate $g_1 \sim 0.41$ THz and $\Gamma_1 \sim 0.75$ GHz.

The strain ε applied along the Ir-O-Ir bond direction [1 1 0] acts differently. It couples to the quadrupole Q_2 of $x^2 - y^2$ symmetry, and thus contributes to the second term in Eq. (2): $\varepsilon_2 \to (\varepsilon_2 + \varepsilon)$. Minimizing the resulting E_{s-l} with respect to the distortions ε_γ and the angle α, we find two distinct regimes. At small values of strain, $|\varepsilon| < \varepsilon_c$, where $\varepsilon_c = \varepsilon_0 \frac{g_1}{g_2} \left(1 - \frac{\Gamma_2}{\Gamma_1}\right)$, the staggered moment and orthorhombic axis gradually rotate from the $45°$ diagonal ([1 0 0] axis) towards the Ir-O-Ir bond direction, as shown in Fig. 4. Specifically, we find $\cos 2\alpha = \varepsilon / \varepsilon_c$, with a slightly different angle β for the distortion axis given by $\tan 2\beta = \frac{\varepsilon_1}{\varepsilon_2 + \varepsilon} = \frac{g_2}{g_1} \tan 2\alpha$. However, the magnetic anisotropy energy curvature is not affected by this rotation, and thus the magnon gap remains unchanged: $\Delta(\varepsilon < \varepsilon_c) = \Delta_0$.

For strain values $|\varepsilon| > \varepsilon_c$, the lattice deformation axis and moment direction stay along the Ir-O-Ir bond direction (see Fig. 4), while the distortion amplitude and hence the magnon gap start to increase. We find

$$\Delta(\varepsilon > \varepsilon_c) = \Delta_0 \sqrt{1 + \frac{g_2}{g_1} \frac{|\varepsilon| - \varepsilon_c}{\varepsilon_0}}. \qquad (8)$$

The theoretical results for $\varepsilon \parallel [110]$ agree well with the data (Fig. 3b). We used the following fit parameters:

$$\begin{aligned} \Delta_0 &= 0.56 \text{ THz}, & \varepsilon_0 &= 1.18 \times 10^{-3}, \\ g_2/g_1 &= 1.43, & \varepsilon_c &= 3.46 \times 10^{-4}, \end{aligned} \qquad (9)$$

where the value of ε_0 is from Eq. (7). With the $\varepsilon_c/\varepsilon_0$ and g_2/g_1 values at hand, we evaluate the ratio $\Gamma_2/\Gamma_1 = 0.58$, in excellent agreement with its estimate (0.6[24]) obtained from the magnetization anisotropy data[26]. Notice that the magnon energy for $|\varepsilon| < \varepsilon_c$ is not perfectly flat and shows rounding of the curve around ε_c. This could be due to local
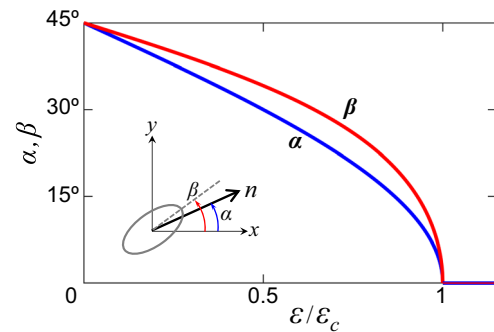

Fig. 4 | Rotation of the staggered moment and orthorhombic axis under uniaxial strain. Angles α and β which specify the staggered moment direction and lattice deformation axis (see inset), correspondingly, as a function of strain ε applied along the [1 1 0] direction.

defects and interfaces between domain boundaries affecting the local potential and, thus, the dynamics of domain rotation and subsequent elongation/compression. Alternatively, the presence of a small magnetic anisotropy could give rise to such rounding of the experimental curve, as discussed in Supplementary Note 2.

Discussion

Overall, the pseudospin-lattice coupling theory accounts very well for our observations, especially the strong anisotropy of the strain effect. The latter is due to the presence of an intrinsic orthorhombicity, which is caused by the same pseudospin-lattice coupling that breaks the tetragonal symmetry of Sr_2IrO_4. From our data, we have quantified this distortion as $\varepsilon_0 \sim 10^{-3}$. Our results call for careful diffraction studies on high-quality single crystals of Sr_2IrO_4 to re-examine its crystal structure, which has so far been regarded as tetragonal. Interestingly, several reports on magnetoresistivity[37] and neutron diffraction[38,39] measurements also imply the presence of orthorhombic distortions in Sr_2IrO_4.

The observed giant response of the magnon energies to uniaxial stress is a direct fingerprint of unquenched orbital magnetism, which is naturally coupled to the crystal environment and provides an effective link between magnetism and lattice deformations. The theory of pseudospin-lattice interactions described here is generally applicable to other correlated-electron systems with spin−orbit-entangled magnetism. For example, it should form a basis for the understanding of magnetoelastic effects in the pseudospin $\widetilde{J} = 1/2$ Kitaev model material $RuCl_3$ and the $\widetilde{J} = 0$ excitonic magnet Ca_2RuO_4.

We end our discussion with a few remarks on the potential of our results for the field of magnonics, which aims to develop high-speed electronic devices with minimal heating losses. The field has recently begun to focus on magnons with characteristic frequencies in the THz regime, which are common in antiferromagnets (including Sr_2IrO_4)[40−42]. However, manipulating the propagation of antiferromagnetic magnons on the requisite nanoscopic length scale presents a formidable challenge. Whereas the magnon energies are, in principle, susceptible to magnetic fields via the Zeeman interaction, it is difficult to engineer magnetic field configurations on this length scale. Analogous constraints apply to electric field manipulation of magnons in multiferroics. The uniaxial strain has been used to manipulate the ground states of complex antiferromagnets[43,44], and some evidence has recently been reported for the sensitivity of ferromagnetic magnons at GHz frequencies to epitaxial[45] or bending strain[46]. The extreme stress sensitivity of THz magnons we have discovered in a simple antiferromagnet opens up new opportunities for guiding magnons via strain domains in an otherwise homogeneous material, without resorting to heteroepitaxy and lithography[47]. Magnon conduits and magnonic crystals could then be fashioned from self-assembled strain domain patterns in thin-film structures, which can be readily reconfigured by

force microscopy. Finally, the unexpectedly large stress response we have observed will greatly enhance the interaction of magnons and surface acoustic waves, which have been proposed as a platform for transient, reconfigurable magnonic crystals[42]. Whereas the feasibility of these design concepts remains to be explored, the results we have presented indicate that the giant stress response mediated by the spin−orbit interaction in $4d$- and $5d$-electron systems offer a powerful tuning parameter for the propagation of terahertz magnons.

Methods

Since the magnetic structure of Sr_2IrO_4 is highly sensitive to chemical defects, high-quality Sr_2IrO_4 crystals were selected following the criteria discussed in the literature[34]. The crystals were cut into a needle shape using a wire saw and clamped into the strain device using the epoxy Stycast 2850FT. The applied stress was controlled by applying voltages on the piezoelectric stacks. The cutting process very often revealed a cleaved surface perpendicular to the c-axis, which is suitable for Raman experiments. All the data presented here were measured on cleaved surfaces. The beam spot of the laser (~$10 \times 10\,\mu m^2$) on the sample is much smaller than the exposed area of the sample (~$600 \times 200\,\mu m^2$), ensuring a homogeneous strain in the probing volume.

The Raman scattering experiments were performed in back-scattering geometry using a JobinYvon LabRAM HR800 spectrometer from HORIBA. The 632.8 nm wavelength of a HeNe laser was chosen as the excitation line to maximize the magnetic scattering signals[25]. All the presented spectra under strain were measured at $T = 20$ K. In order to capture small energy shifts, a diffraction grating with 1800 grooves/mm was used. To avoid any measurement inconsistencies originating from spatial inhomogeneities, the Raman spectra were collected at the same position on the sample throughout the experiment. Due to the geometrical constraints of the experimental setup, the incident polarization was set to be parallel to the strain direction. As a result, depending on the strain direction, a different scattering configuration was required for magnon measurements in the B_{2g}-symmetry: $c(ab)\bar{c}$ (B_{2g}) for [1 0 0] strain and $c(xx)\bar{c}$ ($A_{1g} + B_{2g}$) for [1 1 0] strain.

Data availability

Data that support the findings of this study are available from the corresponding authors upon request.

References

1. Witczak-Krempa, W., Chen, G., Kim, Y. B. & Balents, L. Correlated quantum phenomena in the strong spin-orbit regime. *Annu. Rev. Condens. Matter Phys.* **5**, 57 (2014).
2. Takayama, T., Chaloupka, J., Smerald, A., Khaliullin, G. & Takagi, H. Spin-orbit-entangled electronic phases in $4d$ and $5d$ transition-metal compounds. *J. Phys. Soc. Jpn.* **90**, 062001 (2021).
3. Abragam, A. & Bleaney, B. *Electron Paramagnetic Resonance of Transition Ions* (Clarendon Press, 1970).
4. Khaliullin, G. Orbital order and fluctuations in Mott insulators. *Prog. Theor. Phys. Suppl.* **160**, 155 (2005).
5. Kitaev, A. Anyons in an exactly solved model and beyond. *Ann. Phys.* **321**, 2 (2006).
6. Jackeli, G. & Khaliullin, G. Mott insulators in the strong spin-orbit coupling limit: from Heisenberg to a quantum compass and Kitaev models. *Phys. Rev. Lett.* **102**, 017205 (2009).
7. Chaloupka, J., Jackeli, G. & Khaliullin, G. Kitaev-Heisenberg model on a honeycomb lattice: possible exotic phases in iridium oxides A_2IrO_3. *Phys. Rev. Lett.* **105**, 027204 (2010).
8. Chun, S. H. et al. Direct evidence for dominant bond-directional interactions in a honeycomb lattice iridate Na_2IrO_3. *Nat. Phys.* **11**, 462 (2015).
9. Takagi, H., Takayama, T., Jackeli, G., Khaliullin, G. & Nagler, S. E. Concept and realization of Kitaev quantum spin liquids. *Nat. Rev. Phys.* **1**, 264 (2019).
10. Donnerer, C. et al. All-in-all-out magnetic order and propagating spin waves in $Sm_2Ir_2O_7$. *Phys. Rev. Lett.* **117**, 037201 (2016).
11. Sagayama, H. et al. Determination of long-range all-in-all-out ordering of Ir^{4+} moments in a pyrochlore iridate $Eu_2Ir_2O_7$ by resonant x-ray diffraction. *Phys. Rev. B* **87**, 100403(R) (2013).
12. Shinaoka, H., Hoshino, S., Troyer, M. & Werner, P. Phase diagram of pyrochlore iridates: all-in-all-out magnetic ordering and non-Fermi-liquid properties. *Phys. Rev. Lett.* **115**, 156401 (2015).
13. Bertinshaw, J., Kim, Y. K., Khaliullin, G. & Kim, B. J. Square lattice iridates. *Annu. Rev. Condens. Matter Phys.* **10**, 315 (2019).
14. Kim, B. J. et al. Phase-sensitive observation of a spin-orbital Mott state in Sr_2IrO_4. *Science* **323**, 1329 (2009).
15. Kim, J. et al. Magnetic excitation spectra of Sr_2IrO_4 probed by resonant inelastic X-ray scattering: establishing links to cuprate superconductors. *Phys. Rev. Lett.* **108**, 177003 (2012).
16. Vale, J. G. et al. Importance of XY anisotropy in Sr_2IrO_4 revealed by magnetic critical scattering experiments. *Phys. Rev. B* **92**, 020406(R) (2015).
17. Boseggia, S. et al. Locking of iridium magnetic moments to the correlated rotation of oxygen octahedra in Sr_2IrO_4 revealed by x-ray resonant scattering. *J. Phys. Condens. Matter* **25**, 422202 (2013).
18. Gim, Y. et al. Isotropic and anisotropic regimes of the field-dependent spin dynamics in Sr_2IrO_4: Raman scattering studies. *Phys. Rev. B* **93**, 024405 (2016).
19. Gretarsson, H. et al. Raman scattering study of vibrational and magnetic excitations in $Sr_{2-x}La_xIrO_4$. *Phys. Rev. B* **96**, 115138 (2017).
20. Calder, S., Pajerowski, D. M., Stone, M. B. & May, A. F. Spin-gap and two-dimensional magnetic excitations in Sr_2IrO_4. *Phys. Rev. B* **98**, 220402(R) (2018).
21. Yildirim, T., Harris, A. B., Aharony, A. & Entin-Wohlman, O. Anisotropic spin Hamiltonians due to spin-orbit and Coulomb exchange interactions. *Phys. Rev. B* **52**, 10239 (1995).
22. Skjeltorp, A. & Sherrington, D. *Dynamical Properties of Unconventional Magnetic Systems* (Kluwer Academic, 1998).
23. Katukuri, V. M. et al. Mechanism of basal-plane antiferromagnetism in the spin-orbit driven iridate Ba_2IrO_4. *Phys. Rev. X* **4**, 021051 (2014).
24. Liu, H. & Khaliullin, G. Pseudo-Jahn-Teller effect and magnetoelastic coupling in spin-orbit Mott insulators. *Phys. Rev. Lett.* **122**, 057203 (2019).
25. Gretarsson, H. et al. Two-magnon Raman scattering and pseudospin-lattice interactions in Sr_2IrO_4 and $Sr_3Ir_2O_7$. *Phys. Rev. Lett.* **116**, 136401 (2016).
26. Porras, J. et al. Pseudospin-lattice coupling in the spin-orbit Mott insulator Sr_2IrO_4. *Phys. Rev. B* **99**, 085125 (2019).
27. Kim, J.-W. et al. Controlling symmetry of spin-orbit entangled pseudospin state through uniaxial strain. *Phys. Rev. B* **102**, 054420 (2020).
28. Hicks, C. W., Barber, M. E., Edkins, S. D., Brodsky, D. O. & Mackenzie, A. P. Piezoelectric-based apparatus for strain tuning. *Rev. Sci. Instrum.* **85**, 065003 (2014).
29. Hicks, C. W. et al. Strong increase of T_c of Sr_2RuO_4 under both tensile and compressive strain. *Science* **344**, 283 (2014).
30. Barber, M. E., Gibbs, A. S., Maeno, Y., Mackenzie, A. P. & Hicks, C. W. Resistivity in the vicinity of a van Hove singularity: Sr_2RuO_4 under uniaxial pressure. *Phys. Rev. Lett.* **120**, 076602 (2018).
31. Kim, H.-H. et al. Uniaxial pressure control of competing orders in a high-temperature superconductor. *Science* **362**, 1040 (2018).
32. Kim, H.-H. et al. Charge density waves in $YBa_2Cu_3O_{6.67}$ probed by resonant X-ray scattering under uniaxial compression. *Phys. Rev. Lett.* **126**, 037002 (2021).
33. Steppke, A. et al. Strong peak in T_c of Sr_2RuO_4 under uniaxial pressure. *Science* **355**, 9398 (2017).
34. Sung, N. H. et al. Crystal growth and intrinsic magnetic behaviour of Sr_2IrO_4. *Philos. Mag.* **96**, 413 (2016).

35. Cao, G., Bolivar, J., McCall, S., Crow, J. E. & Guertin, R. P. Weak ferromagnetism, metal-to-nonmetal transition, and negative differential resistivity in single-crystal Sr_2IrO_4. *Phys. Rev. B* **57**, R11039(R) (1998).

36. Fujiyama, S. et al. Two-dimensional Heisenberg behavior of J_{eff}=1/2 isospins in the paramagnetic state of the spin-orbital Mott insulator Sr_2IrO_4. *Phys. Rev. Lett.* **108**, 247212 (2012).

37. Wang, H. et al. Giant anisotropic magnetoresistance and non-volatile memory in canted antiferromagnet Sr_2IrO_4. *Nat. Commun.* **10**, 2280 (2019).

38. Dhital, C. et al. Neutron scattering study of correlated phase behavior in Sr_2IrO_4. *Phys. Rev. B* **87**, 144405 (2013).

39. Ye, F. et al. Magnetic and crystal structures of Sr_2IrO_4: a neutron diffraction study. *Phys. Rev. B* **87**, 140406(R) (2013).

40. Barman, A. et al. The 2021 magnonics roadmap. *J. Phys. Condens. Matter* **33**, 413001 (2021).

41. Zakeri, K. Magnonic crystals: towards terahertz frequencies. *J. Phys. Condens. Matter* **32**, 363001 (2020).

42. Grundler, D. Reconfigurable magnonics heats up. *Nat. Phys.* **11**, 438–441 (2015).

43. Nii, Y. et al. Uniaxial stress control of skyrmion phase. *Nat. Commun.* **6**, 8539 (2015).

44. Haykal, A. et al. Antiferromagnetic textures in $BiFeO_3$ controlled by strain and electric field. *Nat. Commun.* **11**, 1704 (2020).

45. Jeong, S. G. et al. Symmetry-driven spin-wave gap modulation in nanolayered $SrRuO_3/SrTiO_3$ heterostructures: implications for spintronic applications. *ACS Appl. Nano Mater.* **4**, 2160–2166 (2021).

46. Gusev, N. S. et al. Manipulation of the Dzyaloshinskii-Moriya interaction in Co/Pt multilayers with strain. *Phys. Rev. Lett.* **124**, 157202 (2020).

47. Haldar, A. & Adeyeye, A. O. Functional magnetic waveguides for magnonics. *Appl. Phys. Lett.* **119**, 060501 (2021).

Author contributions

Funding

Competing interests

The authors declare no competing interests.

Additional information

Supplementary information The online version contains supplementary material available at https://doi.org/10.1038/s41467-022-34375-6.

Correspondence and requests for materials should be addressed to Huimei Liu, Bernhard Keimer or Matteo Minola.

Peer review information *Nature Communications* thanks Woo Seok Choi and the other, anonymous, reviewer(s) for their contribution to the peer review of this work.

Reprints and permissions information is available at http://www.nature.com/reprints

Publisher's note Springer Nature remains neutral with regard to jurisdictional claims in published maps and institutional affiliations.